Exciton-phonon coupling in individual ZnTe nanorods studied by resonant Raman spectroscopy

Zhang, Q.; Zhang, J.; Utama, M. I. B.; Peng, B.; Mata, Maria de la; Arbiol, Jordi; Xiong, Qihua

2012

Zhang, Q., Zhang, J., Utama, M. I. B., Peng, B., Mata, M. d. l., Arbiol, J., et al. (2012). Exciton-phonon coupling in individual ZnTe nanorods studied by resonant Raman spectroscopy. Physical Review B, 85(8), 085418-.

https://hdl.handle.net/10356/95394

https://doi.org/10.1103/PhysRevB.85.085418

Exciton-phonon coupling in individual ZnTe nanorods studied by resonant Raman spectroscopy

Q. Zhang,[1] J. Zhang,[1] M. I. B. Utama,[1] B. Peng,[1] M. de la Mata,[2] J. Arbiol,[2,3] and Qihua Xiong[1,4,*]

[1]*School of Physical and Mathematical Sciences, PAP 04-14, 21 Nanyang Link, Nanyang Technological University, Singapore 637371, Singapore*

[2]*Institut de Ciència de Materials de Barcelona, ICMAB-CSIC, Campus de la UAB, 08193 Bellaterra, Catalonia, Spain*

[3]*Institució Catalana de Recerca i Estudis Avançats (ICREA), 08010 Barcelona, Catalonia, Spain*

[4]*Division of Microelectronics, School of Electrical and Electronic Engineering, Nanyang Technological University, Singapore 639798, Singapore*

(Received 28 October 2011; revised manuscript received 9 January 2012; published 10 February 2012)

The exciton-phonon coupling in high-quality cubic phase zinc telluride (ZnTe) nanorods (NRs) is investigated by resonant micro-Raman spectroscopy near the direct bandgap of ZnTe. The scattering cross section of longitudinal optical (LO) phonon is enhanced significantly in the resonant process, where the enhancement factor of LO modes is much higher than that of the transverse optical (TO) modes, indicating a dominant Fröhlich electron-phonon interaction mechanism. Up to fifth-order LO phonons are observed by resonant Raman scattering at room temperature. The Huang-Rhys factor of individual NRs—and thus the exciton-LO coupling strengths—is evaluated, showing increasing with the NR diameter. Surface optical (SO) phonon and its high-order overtones are observed between nLO and $(n-1)$LO + TO for the first time, whose positions are consistent with a dielectric continuum model. Strong acoustic phonon-exciton coupling induces a high-frequency shoulder above each nLO peaks with two maxima located around 14 cm^{-1} and 32 cm^{-1}, which are assigned to transverse acoustic and longitudinal acoustic phonons, respectively. The resonant multiphonon scattering process involving acoustic and LO phonons is discussed based on an exciton-intermediated cascade model, where a scattering sequence of acoustic phonon followed by LO phonons is favorable. These results advance the understanding of electron-phonon coupling and exciton scattering in quasi-one-dimensional systems, especially in the scarcely documented ZnTe compound, facilitating the development and optimization of NR-based optoelectronic devices.

DOI: 10.1103/PhysRevB.85.085418 PACS number(s): 78.67.Qa, 78.30.Fs

I. INTRODUCTION

Electron-phonon coupling is an important issue in determining the physical properties of crystalline structures.[1–5] It plays a key role in the transport properties and the relaxation rate of excited carries, thus significantly influencing the electrical and optical properties of the materials. In polar semiconductors such as CdS, CdSe, and ZnO, the free excitons are strongly coupled to longitudinal optical (LO) phonons via the Fröhlich or the polar interaction between the dipolar field induced by the vibrational motion of lattice and the electronic charge density.[6–11] The coupling has been demonstrated to reduce the lifetime of the electronic states significantly, thus leading to broadened linewidths. The near band-edge emission is also modified by the nuclei distortion, resulting in phonon replicas in low temperature fluorescence.[12]

Remarkable progress in material science has made it possible to fabricate semiconductor nanostructures with large surface-to-volume ratio and sizes small enough to be comparable with the characteristic lengths of excitons and free carriers.[13–16] In these materials, the quantum confinement effect and surface effect becomes predominant, resulting in many interesting optical and electronic properties distinct from those of the bulk.[17–26] In the nanoscale regime, in addition to the electronic and vibrational states by themselves, the coupling between electronic and vibrational states is also significantly different from that of bulk counterpart. Understanding of such coupling is essential to rationally tailor the optical properties of nanostructures and improve the performance of optoelectronic devices.

The electron-phonon coupling as a function of the size of nanostructures is still a relevant and controversial topic.[5,27] Theoretically, using a simple charge neutrality argument, Schmitt-Rink and coworkers predicted that the electron-LO-phonon coupling mediated by Fröhlich interaction diminishes with the decreasing size of nanostructures.[28] Klein *et al*., by a donor-like exciton model without considering the electron-hole correlation, demonstrated that the coupling strength for CdSe quantum dots is size-independent.[29] Marini *et al*., based on sophisticated theoretical treatments using the conduction-bands nonparabolicity, found that the coupling strength should increase with the decrease of nanostructure size.[30] Moreover, Nomura and Kobayashi, taking into account the electron-hole correlation and the band nonparabolicity, suggested that the Fröhlich coupling strength would have a minimal point when the size of the structure is 10 nm.[31] On the other hand, a series of experimental studies in ZnO, CdS, and CdSe nanostructures reported that the electron-phonon coupling vanished with decreasing nanocrystal size.[4,9,31,32] However Scamarcio *et al*. reported that the exciton-LO coupling strength of CdS_xSe_{1-x} nanocrystals increased as the diameter was decreased.[10] Very recently, using time-resolved pump/probe technique Kambhampati *et al*. studied size-dependence electron-coupling of CdSe quantum dots (QDs) and proposed that the controversies were due to the disagreements in experimental method conducted and the wavefunctions used to calculate the coupling strength.[33,34] They reported that frequency domain methods measured the coupling between phonon and a photoproduct of a charge-trapped exciton. On the other hand, time domain methods can measure the intrinsic exciton-LO

coupling, which was also proposed previously by Wise and Krauss.[35–37]

Zinc telluride, a II–VI semiconductor, has a direct band gap of 2.26 eV at room temperature and is thus promising for the fabrication of electro-optic devices in pure green region, including green laser generation, light-emitting diode, acousto-optic devices, and photorefractive substrates in optical data processing. Recently, many experimental works have been devoted to the growth and characterization of ZnTe-based structures.[38–40] Due to the lattice mismatch and difference in thermal expansion coefficient with the substrate, most ZnTe layers grown on GaAs/GaSb substrate using molecular beam epitaxy method induces a source of strain and structural defects, hampering the performance of related devices. Moreover, the ZnTe layers exhibit a thickness in micrometer range and area in $\sim mm^2$ range. The optical properties of ZnTe in nanoscale and its size-dependence of electron-phonon interaction are rarely reported.[36] Here we demonstrate the synthesis of high-quality cubic zincblende ZnTe nanorods (NRs) array using van der Waals epitaxy.[41] A comprehensive study of Raman scattering and high-resolution transmission electron microscopy (HRTEM) is presented, strongly demonstrating the existence of Te-aggregate on the surface of NRs. Further we study the exciton-phonon interactions in individual ZnTe NR by resonant Raman scattering (RRS) technique near the energy bandgap. Up to fifth-order LO phonons are indentified in room temperature, which can be addressed principally as a result of Fröhlich interaction. The Huang-Rhys factor, a figure of merit of the electron-phonon coupling strength, of the nanostructure is evaluated as a function of the NR diameter, which increases from 3.2 to 4.8 as the NRs' diameter increased from 90 nm to 200 nm. Besides, surface optical (SO) phonon bands and its high-order overtones have been observed between nLO and (n − 1)LO + transverse optical (TO), whose peak positions are consistent with a dielectric continuum model. Furthermore, due to the exciton-acoustic phonon interaction during exciton recombination process, a high-frequency shoulder is resolved above each nLO peak with two maxima located around 14 cm^{-1} and 32 cm^{-1}, which are assigned to transverse acoustic (TA) and longitudinal acoustic (LA) phonons, respectively. Based on an exciton-intermediated cascade model, acoustic and LO phonons combination scattering near resonant condition is discussed, and the scattering sequence is determined to be acoustic phonon scattering followed by the scattering of LO phonons.

II. SAMPLE PREPARATION

The ZnTe NRs were prepared by a vapor transport method via a van der Waals epitaxy mechanism, which was first attributed in vertically aligned nanowire array with cadmium chalcogenides.[41] The van der Waals epitaxy allows the growth of defect-free epitaxial structures irrespective of the lattice mismatch with the substrate, as the epitaxy is mainly mediated by a van der Waals interaction instead of covalent chemical bonds. Muscovite mica is utilized as a substrate as it satisfies the requirement of weakly reactive surface.[42] Mica is a layered mineral with a pseudohexagonal basal surface, which is readily cleavable as the layers are bound only by van der Waals force and is thus suitable to support the van der Waals epitaxy mechanism.

A freshly air-cleaved (001) muscovite mica was rinsed with acetone. Poly-L-lysine (0.1% w/v) was dispersed on the mica substrate and left for 5 min before the substrate was blow-dried with a N_2 gun.[41] ZnTe powder (99.99%, Alfa Aesar) was used as a source and put into a quartz tube mounted on a single zone furnace (Lindberg/Blue M TF55035C-1). The mica substrate was positioned in the downstream region inside the quartz tube. The tube was evacuated to a base pressure of 2 mTorr, followed by a 30 sccm flow of high purity Ar premixed with 5% H_2 gas. The temperature and pressure inside the quartz tube were set and stabilized to 850 °C and 50 Torr, respectively, for 30 min. Once the system naturally reached room temperature, the samples were collected and subsequently characterized by field-emission scanning electron microscopy (FESEM, JEOL JSM-7001F), x-ray powder diffraction (XRD, Bruker D8 advanced diffractometer, Cu K_α radiation, detector scan configuration), transmission electron microscopy (TEM, JEOL JEM-2010F), and electron energy loss spectroscopy (EELS, GATAN GIF 2001). For Raman experiments, the as-grown sample was ultrasonicated to remove the NRs from the mica substrate, dispersed into an isopropyl alcohol solution, and drop-cast onto silicon substrates. Special care was taken to dilute the NR solution to achieve single-NR measurements. Nonresonant and near-resonant micro-Raman spectra were conducted at room temperature using a Micro-Raman spectrometer (Horiba-JY T64000) in a backscattering configuration. A series of laser lines 632.8 nm (He-Ne laser), 532 nm (solid state green laser), and 514 nm (Ar^+ laser) were used as the excitation sources. The back-scattered signal was collected through a 100× objective, dispersed by 1800 g/mm grating under a triple subtractive mode with a spectra resolution of $\sim$1 cm^{-1}, and recorded by a liquid nitrogen-cooled charge-coupled device detector. The laser power at the sample surface was measured by a power meter through a 10× objective.

Figure 1(a) displays a representative XRD spectrum and an SEM image of ZnTe NRs. From the SEM image it can be seen that the ZnTe NRs are vertically aligned. Only the peaks corresponding to cubic zincblende structure could be found, whose positions are in good agreement with that of their bulk counterparts. From the SEM image, it can be seen that the ZnTe NRs are vertically aligned. Detector scan configuration, with the radiation source fixed at a near grazing incidence angle, is used to minimize penetration into the mica substrate. Thus, only the peaks corresponding to cubic zincblende structure could be found in the XRD pattern, whose positions are in good agreement with that of their bulk counterpart. The diameter appears to change from 80 to 300 nm depending on the position NRs on the substrate. TEM analysis, shown in Figs. 1(b)–1(d), reveals high diameter uniformity over the whole length of NR. Abundant randomly distributed twin boundaries can be resolved from the HRTEM in Fig. 1(c).[41] The corresponding power spectrum is shown in Fig. 1(d). We found that the NRs are grown along the ⟨111⟩ direction. The twin density in the axis of the NR is high and occured throughout the length of the rod (transversal twins, perpendicular to the growth axis).[43] Such an amount of twin boundaries is distributed without any periodicity, leading to different polytypes and thus an increasing diffraction-spots multiplicity.[44] As a consequence,

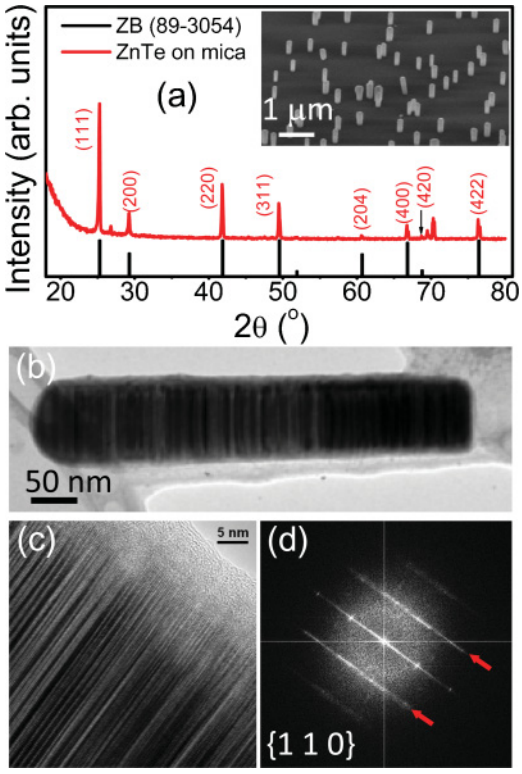

FIG. 1. (Color online) (a) XRD pattern of the ZnTe nanorods (NRs) grown on muscovite mica substrate (blue curve), together with the reference pattern of standard zincblende ZnTe sample (black lines, JCPDS 89-3054). Inset: SEM image of the NRs in a 45° tilted view. (b) A TEM image showing the full length of ZnTe NR. (c) HRTEM image of the NR. (d) The corresponding power spectrum of the image in (c).

the Bragg reflections in the power spectrum appear as a nearly continuous line along the growth direction of the NR instead of isolated spots in the FFT spectrum of periodically twinned superlattices.[45]

III. NONRESONANT RAMAN SCATTERING AND TE ENRICHMENT

The unit cell of cubic zincblende ZnTe contains two atoms. Thus, one would expect three degenerate optical phonon modes at the center of the Brillouin zone ($\boldsymbol{q} = 0$). However, the bonding is partially ionic, and the macroscopic electric field associated with the LO mode lifts the degeneracy, thus leading to the LO-TO splitting. In this case, the first-order Raman spectrum consists of two peaks: The higher frequency mode is denoted as the LO branch and the lower is the doubly degenerate TO branch.[46] Figure 2(a) shows a typical Raman spectrum of an individual ZnTe NR consisting of both Stokes and anti-Stokes contributions. The excitation wavelength and power are 633 nm and 0.2 mW, respectively. The TO Raman peak is located at 175 cm^{-1} with a full width at half maximum (FWHM) of 3.4 cm^{-1}, and the LO Raman peak is located at 205 cm^{-1} with a FWHM of 4.2 cm^{-1}, which are consistent with previous Raman scattering studies on ZnTe.[47,48] No higher order optical phonon scattering was observed by 633 nm excitation.

Below the TO Raman peak, three low frequency vibrational modes are observed: 110 cm^{-1}, 120 cm^{-1}, and 145 cm^{-1}. Similar features have also been observed in other telluride compounds such as CdTe.[49–51] Until now, the origin of the low-frequency features was unclear. Generally, those low frequency features were believed to be associated with Te-aggregate or inclusions due to the lack of stoichiometry or poor tellurium bonding as a result of growth and atmosphere oxidation.[49–51] In some earlier Raman scattering studies on ZnTe, these modes were assigned to second-order Raman scattering with phonon frequencies at the zone boundary of W critical point.[48] Later studies by Kuhn *et al*. demonstrated that the low frequency could be associated with the Te phase along ZnTe surface.[38] Since the Raman spectrum of amorphous Te is dominated by a broad band, the sharp peaks around 110 cm^{-1}, 120 cm^{-1}, and 145 cm^{-1} are normally assigned to E_{LO}, A_1, and E_{LO}/E_{TO} modes of the crystalline Te phase, respectively.[51,52] Figure 2(b) shows the Raman scattering spectra at higher laser power excitation. The intensity of the Te modes was enhanced with the increase of laser power and became much stronger than TO and LO peaks of ZnTe when the laser power was 2.0 mW. The laser-induced effect was also observed in other Te composites and suggests the formation of crystalline Te aggregates due to the damage from laser irradiation.[50] According to energy dispersive spectroscopy (EDS) study by Larramendi *et al*., the chemical transformation happening on the surface of ZnTe NR was due to some complicated photo-chemical reactions in Te composites.[53] Traditionally, the local temperature T can be estimated by the ratio of anti-stokes and stokes scattering intensity. However, considering that the ZnTe amount was decreased due to photoreaction during the lasing exposure, we estimated the T based on the relation between LO frequency ω_{LO} and T ($d(\ln\omega_{LO})/dT = -4 \times 10^{-5}/K$).[54] The local sample temperature was around 180 °C when the excitation power was 0.6 mW, which is much lower than the melting point of ZnTe (1238 °C). Therefore, the laser-induced composition change is probably not due to the evaporation of Zn or any heating effect but photo-chemical reactions involved in hole or vacancy migrations.[55]

To further study Te-rich aggregation mechanism in telluride compounds, we performed a detailed EELS and high angle annular dark field scanning transmission electron microscopy (HAADF-STEM) analysis, which strongly supported the result in Raman scattering. Figure 2(c) displays a HAADF STEM image of a ZnTe NR (left) and the corresponding areal density maps of the principal elements (middle). Besides Zn and Te, O was detected mainly around the NRs and especially in the bottom surface, which may be attributed to the oxidation process (TeOx) and contribution from the mica substrate, which may also be cleaved during ultrasonication. To detect possible compositional variation, we calculate the relative composition of Zn and Te in different regions of the NR without taking into the account of oxygen, as shown in the right sub-Fig. 2(c). The atomic composition of Zn and Te is kept along the rod (1:1 ratio), within the experimental error (estimated to be the ±5%). Nevertheless, the tip and the base of the NR are both Te rich. Notice that these two points correspond with the NR surface. Thus, the NR is surrounded by a tellurium-rich material (in addition to the oxygen), which explains why the Te signal is slightly higher than the Zn

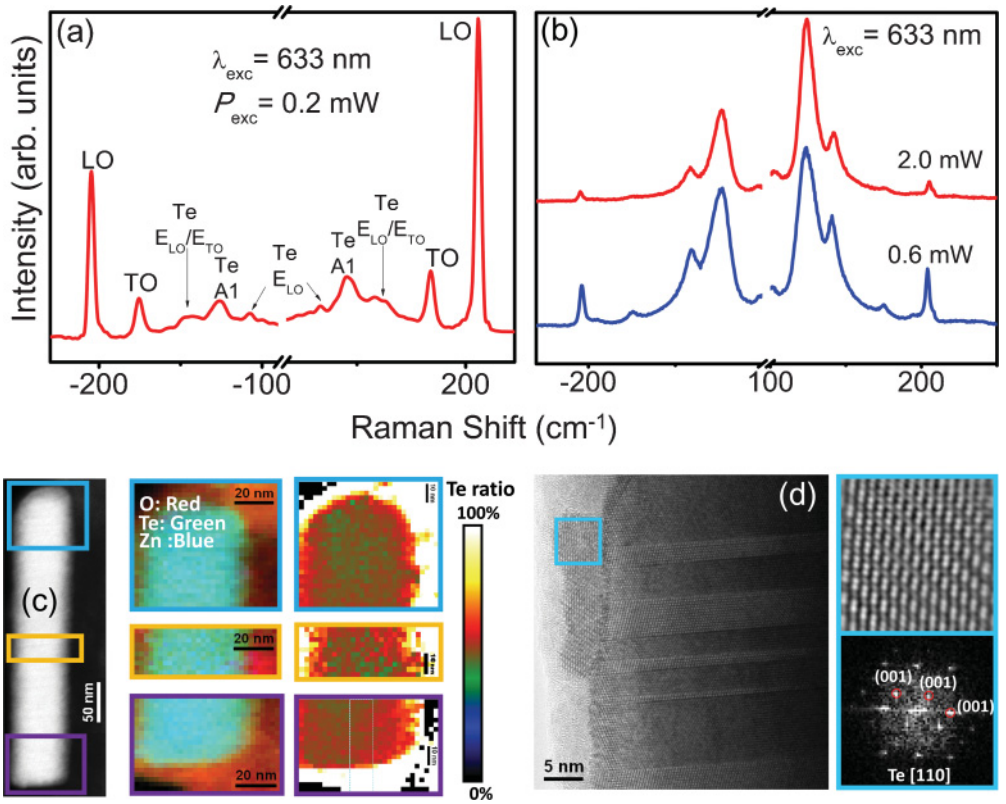

FIG. 2. (Color online) (a) Raman scattering spectrum of individual ZnTe nanorod (NR). The excitation wavelength is 633 nm and the power is 0.2 mW. (b) The corresponding Raman scattering spectra when the ZnTe NR is excited with 0.6 mW (blue/medium gray curve) and 2.0 mW (red/dark gray curve) laser power. (c) HAADF-STEM of a ZnTe rod (left); EELS map of the ZnTe NR obtained from three areas that are marked in the left figure with rectangles with different colors (middle). The signal from the elements are color-coded as red/dark gray for O, green/gray for Te, and blue/medium gray for Zn; the EELS map of Zn and Te elemental ratio without considering O, where the color in the vertical bar represents the Te ratio (right). (d) HRTEM of a ZnTe NR (left); zoom-in image (right, upper) and the power spectrum (right, lower) of Te-aggregate on the surface of the ZnTe NRs, which is marked with a cyan/medium gray square in the left figure.

signal. Figure 2(d) shows the HRTEM images around the surface of a NR, clearly showing a particle aggregate on the surface. The particle shows a good single crystallization, as shown in the high magnification HRTEM image and the power spectrum of the area marked with a cyan square. The lattice has a zig-zag structure consisting of atomic chains corresponding to metallic tellurium, which crystallizes in a hexagonal structure, in agreement with the pattern from the power spectrum. According to the study by Larramendi *et al.*,[53] the laser-induced Te-aggregate effect has an excitation power threshold of 4.4×10^5 W/cm^2. Thus, we do not expect damage before the TEM studies. In this case, the Te-aggregation most likely occurs during the growth process.

IV. RESONANT RAMAN SCATTERING AND FRÖHLICH INTERACTION

RRS is a fast and effective technique to detect electron-phonon interaction in semiconductor and other materials such as carbon nanotubes, superconductors, etc.[2,11,56,57] Although Fröhlich-induced electron-phonon coupling in the ensemble of nanostructures has been previously investigated under resonance conditions, such ensemble approach is nevertheless not adequate to elucidate the size-dependent electron-phonon coupling. Figures 3(a) and 3(b) show the Raman spectra of individual ZnTe NRs at room temperature excited by 532 nm and 514 nm laser, respectively. The laser power is 0.17 mW in both cases. The strongest Te peaks located at 120 cm^{-1} and 145 cm^{-1} can be resolved. Up to fourth-order LO Raman peaks of ZnTe are clearly observed when the excitation wavelength is 532 nm, and the fifth-order LO peaks can be resolved when the excitation is 514 nm. The frequency of the nLO phonon modes (up to $n = 5$) are 205 cm^{-1}, 410 cm^{-1}, 615 cm^{-1}, 820 cm^{-1}, and 1025 cm^{-1} for $n = 1, 2, 3, 4, 5$, respectively. Those values are multiples of $\omega_{LO} = 205$ cm^{-1},[48] indicating that the multiphonon process is significantly contributed from the Γ point.

The electron-phonon coupling is generally originated from two mechanisms: the deformation potential and the Fröhlich potential. Following Loudon, Kaminow, and Johnston,[58,59] the TO Raman scattering cross section is determined by the deformation potential that involves the short-range interaction between the lattice displacement and the electrons.[26] On the other hand, the LO Raman scattering cross section includes the contributions from both the deformation potential and the Fröhlich potential, the latter of which involves the long-range interaction generated by the displacement of the partially ionic nuclei.[26] In our case, the LO phonons are greatly enhanced by the resonant process, but the TO phonons are almost insensitive. Therefore, we believe that the exciton-phonon

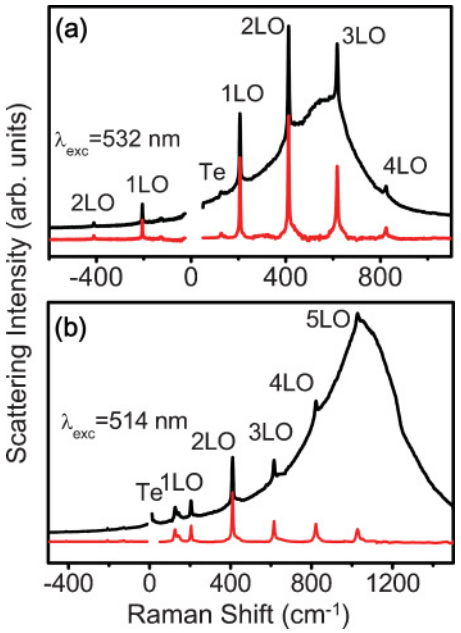

FIG. 3. (Color online) Resonant Raman spectra of individual ZnTe nanorods (NRs) taken in room temperature. The excitation power is 0.17 mW. The excitation wavelength is 532 nm (a) and 514 nm (b). The black and red/dark gray curves are original and PL subtracted spectra, respectively.

coupling in the ZnTe NRs studied in this paper is mainly associated with the Fröhlich interaction.

V. HUANG-RHYS FACTOR AND SIZE-DEPENDENT RAMAN SCATTERING

The coupling strength of the electron-phonon interaction can be evaluated by comparing the relative intensities of the overtones to the fundamental Raman band. According to the Albrecht A term, the Raman scattering cross section for an nth phonon process is given by

$$|R^n(\omega)|^2 = \mu^4 \left| \sum_{m=0}^{\infty} \frac{\langle n|m\rangle\langle m|0\rangle}{E_{\rm ex} + n\hbar\omega_{\rm LO} - \hbar\omega_0 + i\Gamma} \right|^2, \quad (1)$$

where μ is the electronic transition dipole moment, ω_0 is the incident photon frequency, m denotes the intermediate vibration level in the excited state, $E_{\rm ex}$ is electronic transition energy, and Γ is the homogeneous linewidth of electronic state.[26] The Franck-Condon overlap integral $\langle n|m\rangle$ between the ground and excited states can be expressed as[4]

$$\langle n|m\rangle = \left(\frac{n!}{m!}\right)^{1/2} \exp\left(-\frac{1}{2}\Delta^2\right)\Delta^{n-m} L_m^{n-m}(\Delta^2), \quad (2)$$

where L is the associated Laguerre polynomial, and Δ is the dimensionless displacement for the Fröhlich interaction. In general, the exciton-phonon coupling strength can be evaluated by Huang-Rhys parameter S, which can be expressed as[60] $S = \Delta^2/2$. From Eqs. (1) and (2), one can see that S can be determined by measuring the ratio of the integrated intensities of different overtones.

Figure 4(a) shows the RRS of ZnTe NR as a function of NR diameter when they are excited by a 532-nm laser, where

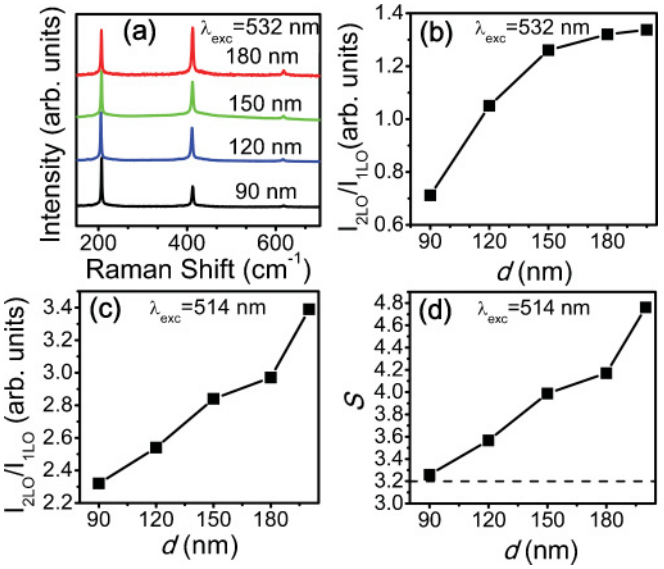

FIG. 4. (Color online) (a) Resonant Raman spectra of individual ZnTe nanorod (NR) with different diameter d: 90 nm (black curve), 120 nm (blue/medium gray curve), 150 nm (green/gray curve), and 180 nm (red/dark gray curve); the excitation wavelength is 532 nm. (b), (c) The integrated intensity ratio of 2LO overtone to 1LO overtone as a function of d, the excitation wavelength is 532 nm (b) and 514 nm (c). (d) Calculated Huang-Rhys factor, S, for individual NR with different d, based on the integrated intensity ratio of 2LO peak to 1LO peak as shown in (c).

the spectra are shifted upwards for clarity. Spectra range is selected from 180 cm^{-1} to 630 cm^{-1} to give a clear view on LO and 2LO Raman peaks. For thin NR (d = 90 nm), 1LO intensity is stronger than that of 2LO. As d increases, 2LO is enhanced and becomes even stronger than 1LO phonon at a diameter of 180 nm. The integrated intensity ratio of 2LO phonon and 1LO phonon as a function of diameter is plotted in Figs. 4(b) and 4(c). While the diameter d increased from 80 nm to 200 nm, the 2LO/1LO intensity ratio increases from 0.3 to 1.2 and from 2.3 to 3.3 when the NR is excited by 532 nm and 514 nm, respectively. The size-dependent intensity ratio is not due to resonant condition tuning effects based on quantum confinement effect. The NR diameter is from 90 nm to 200 nm and much larger than ZnTe exciton Bohr radius (5.2 nm). In these sizes the quantum confinement effect should be too weak to change the bandgap.[61,62] It can also be supported by experimental data that the measured photoluminescence (PL) peaks of all samples are located at ∼(545 ± 1) nm corresponding to the bandgap of bulk ZnTe materials (data not shown here).

Combining Eqs. (1) and (2), the intensity ratio of 2LO to 1LO can be written as[63]

$$\left|\frac{I_{\rm 2LO}}{I_{\rm 1LO}}\right| = \frac{S}{2}\frac{(E_{\rm ex} + \hbar\omega_{\rm LO} - \hbar\omega_0)^2 + \Gamma^2}{(E_{\rm ex} + 2\hbar\omega_{\rm LO} - \hbar\omega_0)^2 + \Gamma^2}. \quad (3)$$

We consider that the LO cross section of ZnTe in resonant condition is dominantly contributed from free excitons, as discussed in the case of CdS.[11,63] At room temperature, the free exciton-binding energy is 13 meV and the bandgap of ZnTe is 2.28 eV, as indicated by the PL backgrounds of Raman spectra in Figs. 3(a) and 3(b), such that exciton energy $E_{\rm ex}$ = 2.25

eV. The exciton linewidth Γis estimated to be about 65 meV[64] according to previous temperature-dependent PL studies in ZnTe layers.[39] The accuracy of the estimation is evidenced by two factors. First, the linewidth would not change much for ZnTe nanostructures with different shape and size or from a sample grown by different methods. Moreover, the systematic analysis performed by Krauss *et al*. suggests that the variation of Γ does not have a strong influence on the S, and the resulting error is small when we calculate S from the intensity ratio of 2LO to 1LO.[36] As Fig. 4(d) shows, S increases from 3.2 to 4.8 as the diameter increases from 90 nm to 200 nm. The measured size-dependence of exciton-LO phonon coupling strength is consistent with previous studies in the ZnO nanowire and CdS nanocrystal.[4,9,31,32] In those studies, the confinement of electron and hole was considered to be responsible for the relationship.[28] For the excitons in bulk crystal, the electron is more delocalized than the hole. As a result, the lattice experiences a negative charge in the outer region of exciton, but a positive charge in the inner region of exciton. The charges couples to the lattice vibration via Fröhlich interaction.[63] As the electron and hole are confined into a smaller volume, the electron-hole overlap is enhanced. Therefore the electric field caused by lattice vibration would be less effective in polarizing the exciton and thus the Fröhlich coupling strength should vanish.

For bulk ZnTe, the Huang-Rhys parameter S for the Fröhlich interaction is derived by Merlin *et al*. as[65]

$$\Delta^2 = \left(\frac{24}{\pi}\right)^{1/3} \frac{e^2}{a_0 h\omega_{\mathrm{LO}}} \left(\frac{1}{\varepsilon_\infty} - \frac{1}{\varepsilon_0}\right) \frac{1}{w} \int_{x=0}^{w} \frac{x^4(2+x^2)^2}{(1+x^2)^4} dx, \tag{4}$$

which can be written as simply

$$\Delta^2 = \frac{2.16 \times 10^5}{a_0 \omega_{\mathrm{LO}}} \left(\frac{1}{\varepsilon_\infty} - \frac{1}{\varepsilon_0}\right) \frac{1}{w} \int_{x=0}^{w} \frac{x^4(2+x^2)^2}{(1+x^2)^4} dx, \tag{5}$$

where $w = (3\pi^2)^{1/3}(a_0/a_{\mathrm{b}})$, with a_0 and a_{b} being the lattice constant and exciton Bohr radius, respectively. ε_∞ and ε_0 are the high frequency and static dielectric constants, respectively. One thing should be noted: in Eq. (5) the unit of phonon frequency ω_{LO} and lattice constant a_0 is cm^{-1} and Å, respectively. At room temperature, $a_0 = 6.1$ Å, $a_{\mathrm{b}} = 5.2$ nm, $\varepsilon_\infty = 7.28$, and $\varepsilon_0 = 10.1$.[47,66] Substituting the parameters into Eq. (5), the Huang-Rhys factor S for bulk ZnTe is 3.2. This value is smaller than that of ZnTe NR with a diameter of 200 nm (4.8), which may be due to the charge-trapping effect. According to state-resolved and steady-state exciton-phonon coupling studies by Wise, Krauss, and Kambhampati, the photo-generated charge carrier is highly confined and localized in strong confined systems.[35,36,67,68] During the steady-state Raman measurement, the trapped charge would build up on the QDs, produce a local electric field, and thus polarize the exciton. As a result the coupling between exciton and phonons will be strengthened significantly and can be considered as an extrinsic coupling. In PbS QDs, the extrinsic coupling was found to be up to four orders stronger than the intrinsic coupling.[36] For ZnTe NRs with a diameter from 90 nm to 200 nm, the extrinsic coupling strength is found to be around 1.5 times of the intrinsic coupling; therefore, it is reasonable to conclude that the charge carrier confinement effect is much weaker in our ZnTe NRs.

VI. SURFACE OPTICAL PHONON

The Raman spectra around 1LO and 2LO peaks were fitted using multiple Lorentzian functions, as shown in Figs. 5(a)–5(d). Besides the nLO peaks, TO + $(n-1)$LO zone-center phonon combinations can also be resolved below nLO Raman peaks.[40] In addition to the strong nLO and TO + $(n-1)$LO peaks, we observed a broadband and a pronounced high-frequency shoulder of the LO peak between TO and LO peaks. The low-frequency broadband can be well fitted with a Lorentzian profile centered at 199.6 cm^{-1} and with a FWHM of 20 cm^{-1}. Position of the broadband shows no apparent shift in Raman axis when the NR is excited by 514 nm and 532 nm lasers, indicating that the broadband is not due to recombination of electronic states but some other quasiparticles. Considering the broadband position (between TO and LO modes) and the large surface-to-volume ratio for NRs, we assigned it to SO modes tentatively. For an infinite cylindrical nanowire, the dispersion relation of SO modes $\omega_{\mathrm{SO}}(q)$ is related to the LO and TO modes[17,69–71]:

$$\omega_{\mathrm{SO}}^2 = \omega_{\mathrm{TO}}^2 + \frac{\tilde{\omega}_p^2}{\varepsilon_\infty + \varepsilon_m f(qr)}, \tag{6}$$

where $\tilde{\omega}_p$ is the screened ion plasma frequency given by $\omega_{\mathrm{LO}}^2 = \omega_{\mathrm{TO}}^2 + \tilde{\omega}_p^2/\varepsilon_\infty$; r is the NR radius; ε_m is dielectric constant of medium; and $f(qr)$ is a function obtained from the eigenvalue equation

$$f(qr) = \frac{I_0(qr)K_1(qr)}{I_1(qr)K_0(qr)}. \tag{7}$$

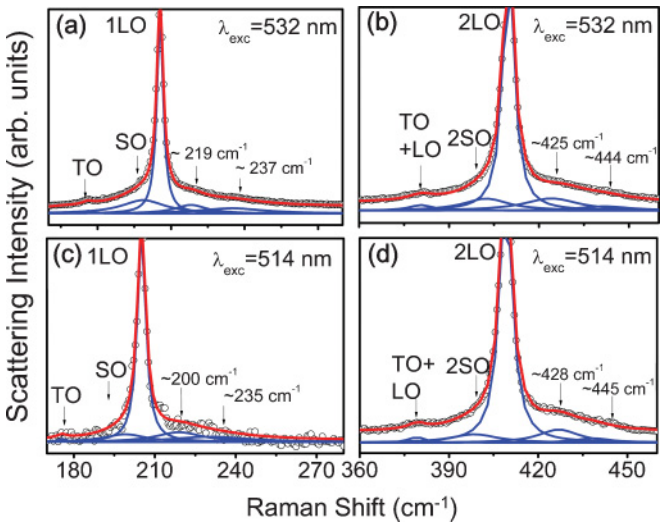

FIG. 5. (Color online) Representative fits of resonant Raman scattering spectra around 1LO and 2LO peaks of ZnTe nanorods (NRs). (a), (b) Resonant Raman scattering spectra when the excitation wavelength is 532 nm. The spectra range is around 1LO in (a) and 2LO in (b). (c), (d) Resonant Raman scattering spectra when the excitation wavelength is 514 nm. The spectra range is around 1LO in (c) and 2LO in (d).

Here, $I(qr)$, $K(qr)$ are modified Bessel functions. For infinite-diameter cylinders, $r \to \infty$, $f(qr) \to 1$, thus,

$$\omega_{SO} = \omega_{TO}\sqrt{\frac{\varepsilon_0 + \varepsilon_m}{\varepsilon_\infty + \varepsilon_m}}. \quad (8)$$

Substituting $\omega_{TO} = 175\ \mathrm{cm}^{-1}$, $\varepsilon_m = 1$ (air), $\varepsilon_\infty = 7.28$, and $\varepsilon_0 = 10.1$ into Eq. (8), ω_{SO} is 202.6 cm^{-1} ($r \to \infty$). However, for ZnTe NR with r of 40 $\sim$ 100 nm, $f(qr)$ is larger than 1, therefore SO band frequency should be smaller than 202.6 cm^{-1}, which is in good agreement with our experiment result. According to Eqs. (6) and (7), it appears that values of the SO band frequency calculated for $qr = 2.0$ ($f(qr) = 1.73$) is close to the experimentally obtained value (199.6 cm^{-1}). Considering $r = 75$ nm, the SO wavevector $q \approx 2.6 \times 10^7\ \mathrm{cm}^{-1}$. Besides the fundamental SO mode, the 2SO also can be resolved in our RRS spectra with a center located around 400.3 cm^{-1}, as Fig. 5 shows. This multi-SO scattering also is attributed to an amplified scattering cross-section in RRS situation.

VII. EXCITON ACOUSTIC PHONON COUPLING

The high-frequency part appears as a continuous wing up to 40−50 cm^{-1} above the nLO peaks ($n = 1, 2, 3, 4, 5$). The feature cannot be indentified with surface tellurium, tellurium oxide, or sum phonon modes of ZnTe. Moreover, the feature cannot be well fitted with a reasonably small set of Lorentzian or Gaussian profiles. At a closer look, the wing seemed to be structured with two slightly protruding maxima at about 219 cm^{-1} and 237 cm^{-1} for 1LO peak, while at 425 cm^{-1} and 444 cm^{-1} for 2LO peak. The positions of the maxima exhibited a very small shift (∼2 cm^{-1}) for two excitation wavelengths, which may be attributed to fitting errors. The frequency spacing between the maxima and corresponding nLO peak is almost the same. Taking Raman spectra of 532 nm excitation, for instance, the spacing between 1LO mode and the first maxima of 1LO-sideband is 14 cm^{-1}, which is very close to that for 2LO mode (15 cm^{-1}). The good consistency supports that the nLO high-frequency sidebands are from a multiphonon process. The argument can also be demonstrated by the variation of sideband's intensity as n, and excitation wavelengths are changed. When the energy difference between nLO and exciton ($E_{ex} - n\hbar w_{LO} - \hbar w_0$) is smaller, the intensity of the high-frequency shoulder is stronger. The trend is similar to that of nLO phonons themselves. When the excitation wavelength is 514 nm, the high-frequency shoulder around 1LO peak can rarely be resolved, in contrast to its strong intensity around 2LO. When the excitation wavelength was 532 nm, the high-frequency shoulder around each nLO peaks was resolved.

A similar high-frequency shoulder was recently observed for CdSe NPs and CdTe NPs in room temperature, which was assigned to contribution of acoustic phonons.[8,72–75] Acoustic phonons are involved in most of the electronic processes via deformation potential and piezoelectric potential.[76,77] The exciton-acoustic phonon coupling decides the homogenous exciton linewidth of semiconductor in low temperature and exciton dephasing times. Due to the coupling of a continuum of acoustic-phonon, the emission of exciton exhibits an asymmetric shape with low-frequency sidebands.[78] Besides the exciton-acoustic phonon coupling, electron energy level spacing due to confinement effect can induce the unusual Raman bands.[79] Using the "particle in box" model, the energy level spacing is estimated to be around 0.19 meV ($n_{ex} = 1$) and 0.32 meV ($n_{ex} = 2$), even for a NR with a diameter of 90 nm, n_{ex} is the quantum number of exciton.[80,81] The spacing energy is much smaller than that of experimental observed modes 1.7 meV (12 cm^{-1}) and 3.9 meV (32 cm^{-1}). Therefore, we consider the unusual sidebands are due to acoustic phonon scatterings.

In our case, the acoustic phonon contribution may occur via two mechanisms. The first mechanism can be discussed in terms of combination modes due to a sequential scattering on optical phonon and a continuum of acoustical phonon near Γ point, satisfying the $\boldsymbol{q} = 0$ momentum selection rule for Raman spectra measurement, i.e., nLO + mLA, nLO + mTA, etc. A series of acoustic phonons would be involved and the acoustic phonon's energy is very small, resulting in a high-frequency shoulder. However, the combination modes are rarely reported in II–VI semiconductors.[72] The second mechanism is based on the energy relaxation of the exciton serving as an intermediate state in the present case of the RRS. Due to the strong exciton-acoustic phonon coupling, the exciton can dissipate a part of its energy via scattering of acoustic phonons during a characteristic time of the exciton-LO phonon interaction.[7,8] As a result, the scattering by the LO phonon of such statistical lower energy excitons can produce a descending wing toward higher frequency.

The two maxima of the shoulder (14 cm^{-1} and 32 cm^{-1}) are assigned to 1TA and 1LA modes, whose positions are close to the resonant 1LO and acoustic phonon Raman scattering study by Oka and Cardona.[7] Following the acoustic phonon dispersion curves of ZnTe,[46,47] we estimated the corresponding the TA and LA phonon wavevector $\boldsymbol{q}_{TA} = 1.3\times10^7\ \mathrm{cm}^{-1}$ ($\omega_{TA} = 14\ \mathrm{cm}^{-1}$) and $\boldsymbol{q}_{LA} = 1.3\times10^7\ \mathrm{cm}^{-1}$ ($\omega_{LA} = 32\ \mathrm{cm}^{-1}$). The wavevector is about 1/8 of Brillouin-zone value at X point ($2\pi/a = 1.0 \times 10^8\ \mathrm{cm}^{-1}$), which is in good agreement with previous studies.[82]

Usually, the acoustic phonon-exciton coupling of semiconductor near exciton resonance ($E_0 \sim E_{ex} + \hbar\omega_{LO}$) was discussed using polariton model.[7] In this model the excitonic polartion is scattered from a photonlike branch to excitonic branch by acoustic phonons. However, the model is not effective for describing high-order LO process ($E_0 \sim E_{ex} + n\hbar\omega_{LO}$). The acoustic phonon sidebands can still be resolved when the sample is excited by a 514-nm laser ($E_0 \sim E_{ex} + 5\hbar\omega_{LO}$). Therefore, here we use the exciton-intermediated cascade model to describe the exciton-acoustic-LO scattering processes.[83] In general LO multiphonon cascade process is displayed in Fig. 6(a): a photon (energy ω_0) excites the crystal, inducing a virtual exciton while the photon is destroyed; then a LO-phonon is emitted and the virtual exciton is scattered to a real parabolic dispersive exciton state and the momentum was lowered; next, this real exciton recombines, and a scattered photon is emitted ($\omega_s = \omega_0 - \omega_{LO}$) or is scattered by a second LO-phonon and transited to a lower momentum state along the parabolic curve. This cascade process continues until the exciton momentum approaches a $\boldsymbol{q} = 0$ point. When there is a strong acoustic phonon-exciton interaction, acoustic phonon is involved in this cascade process. Figures 6(b) and 6(c) present

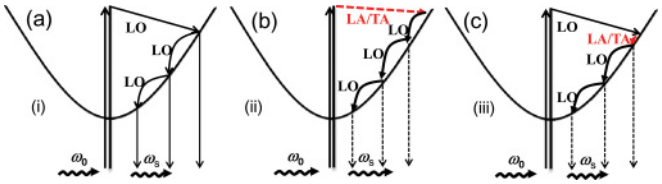

FIG. 6. (Color online) Schematic diagram of acoustic and LO phonon scattering process under resonant condition. (a) Process (i): general multi-LO phonon scattering process. (b) Process (ii): acoustic phonon scattering process followed by LO phonons. (c) Process (iii): LO phonon scattering followed by acoustic phonon.

two possible sequences of acoustic and LO phonon scattering process. In process (ii), acoustic phonon scattering is followed by nLO phonons, however, in process (iii) the situation is inverse. We consider that process (ii) is more favorable than process (iii). First, the momentum and energy of transitions in process (ii) can be conserved so that the scattering can be a step-wise process.[8] In the studies on acoustic and LO phonons in CdS and CdSe, the acoustic phonon scattering was found to be before that of LO phonons.[8,82] Second, if on the basis of that LO scattering is followed by acoustic phonon, it is very possible that the acoustic phonon scattering happens after each LO phonon scattering. The position and shape of acoustic phonon sidebands will not be the same for each LO overtone as a result. However, experimentally the TA/LA position around each nLO peak did not move much.

VIII. CONCLUSION

We investigate the exciton-phonon interaction in high-quality ZnTe NR synthesized by a van der Waals epitaxy mechanism. Fifth-order LO phonons are observed at room temperature due to a strong exciton-LO Fröhlich coupling. As NR diameter decreases from 200 nm to 90 nm, the Huang-Rhys factor S decreases from 4.8 to 3.2. SO and 2SO bands located at 199.6 cm^{-1} and 400.3 cm^{-1} are observed, showing good agreement with theory. Moreover, the nLO phonon peaks exhibit unusual high-frequency wings due to LO + acoustic phonon scattering. The probable scattering sequence is proposed, and acoustic phonon scattering followed by LO phonons is determined.

ACKNOWLEDGMENTS

Q.X. thanks the strong support from Singapore National Research Foundation through Singapore 2009 NRF fellowship grant (NRF-RF2009-06) and Competitive Research Program (NRF-CRP-6-2010-2). He also acknowledges the very strong support from Nanyang Technological University via start-up grant (M58110061) and New Initiative Fund (M58110100). M.M. and J.A. acknowledge funding from the Spanish MICINN projects MAT2010-15138 (COPEON) and CSD2009-00013 (IMAGINE) and Generalitat de Catalunya projects 2009-SGR-770 and XaRMAE.

*qihua@ntu.edu.sg

[1] A. Das, S. Pisana, B. Chakraborty, S. Piscanec, S. K. Saha, U. V. Waghmare, K. S. Novoselov, H. R. Krishnamurthy, A. K. Geim, A. C. Ferrari, and A. K. Sood, Nat. Nanotechnology **3**, 210 (2008).
[2] V. Perebeinos, J. Tersoff, and P. Avouris, Phys. Rev. Lett. **94**, 027402 (2005).
[3] G. D. Gaspari and B. L. Gyorffy, Phys. Rev. Lett. **28**, 801 (1972).
[4] A. P. Alivisatos, T. D. Harris, P. J. Carroll, M. L. Steigerwald, and L. E. Brus, J. Chem. Phys. **90**, 3463 (1989).
[5] A. M. Kelley, ACS Nano **5**, 5254 (2011).
[6] M. V. Klein and S. P. S. Porto, Phys. Rev. Lett. **22**, 782 (1969).
[7] Y. Oka and M. Cardona, Solid State Commun. **30**, 447 (1979).
[8] P. Y. Yu, Solid State Commun. **19**, 1087 (1976).
[9] R. P. Wang, G. Xu, and P. Jin, Phys. Rev. B **69**, 113303 (2004).
[10] V. Spagnolo, G. Ventruti, G. Scamarcio, M. Lugara, and G. C. Righini, Superlattices Microstruct. **18**, 113 (1995).
[11] J. F. Scott, R. C. C. Leite, and T. C. Damen, Phys. Rev. **188**, 1285 (1969).
[12] X. L. Xu, Y. Zhao, E. J. Sie, Y. Lu, B. Liu, S. A. Ekahana, X. Ju, Q. Jiang, J. Wang, H. D. Sun, T. C. Sum, C. H. A. Huan, Y. P. Feng, and Q. H. Xiong, ACS Nano **5**, 3660 (2011).
[13] W. Lu and C. M. Lieber, J. Phys. D **39**, R387 (2006).
[14] S. M. Reimann and M. Manninen, Rev. Mod. Phys. **74**, 1283 (2002).
[15] B. Ketterer, M. Heiss, E. Uccelli, J. Arbiol, and A. Fontcuberta i Morral, ACS Nano **5**, 7585 (2011).
[16] E. Uccelli, J. Arbiol, J. R. Morante, and A. Fontcuberta i Morral, ACS Nano **4**, 5985 (2010).
[17] Q. H. Xiong, J. G. Wang, O. Reese, L. Voon, and P. C. Eklund, Nano Lett. **4**, 1991 (2004).
[18] B. Liu, R. Chen, X. L. Xu, D. H. Li, Y. Y. Zhao, Z. X. Shen, Q. H. Xiong, and H. D. Sun, J. Phys. Chem. C **115**, 12826 (2011).
[19] J. Zhang, Z. P. Peng, A. Soni, Y. Y. Zhao, Y. Xiong, B. Peng, J. B. Wang, M. S. Dresselhaus, and Q. H. Xiong, Nano Lett. **11**, 2407 (2011).
[20] R. Chen, M. I. B. Utama, Z. P. Peng, B. Peng, Q. H. Xiong, and H. D. Sun, Adv. Mater. **23**, 1404 (2011).
[21] R. Chen, D. H. Li, B. Liu, Z. P. Peng, G. G. Gurzadyan, Q. H. Xiong, and H. D. Sun, Nano Lett. **10**, 4956 (2010).
[22] M. W. Cole, V. H. Crespi, M. S. Dresselhaus, G. Dresselhaus, J. E. Fischer, H. R. Gutierrez, K. Kojima, G. D. Mahan, A. M. Rao, J. O. Sofo, M. Tachibana, K. Wako, and Q. H. Xiong, J. Phys. Condes. Matter **22**, 25 (2010).
[23] L. Voon, Y. Zhang, B. Lassen, M. Willatzen, Q. H. Xiong, and P. C. Eklund, J. Nanosci. Nanotechnol. **8**, 1 (2008).
[24] X. F. Liu, R. Wang, Y. P. Jiang, Q. Zhang, X. Y. Shan, and X. H. Qiu, J. Appl. Phys. **108**, 4 (2010).
[25] Q. Zhang, X. Y. Shan, L. Zhou, T. R. Zhan, C. X. Wang, M. Li, J. F. Jia, J. Zi, Q. Q. Wang, and Q. K. Xue, Appl. Phys. Lett. **97**, 3 (2011).
[26] A. C. Albrecht, J. Chem. Phys. **34**, 1476 (1961).
[27] A. M. Kelley, J. Phys. Chem. Lett. **1**, 1296 (2010).
[28] S. Schmitt-Rink, D. A. B. Miller, and D. S. Chemla, Phys. Rev. B **35**, 8113 (1987).
[29] M. C. Klein, F. Hache, D. Ricard, and C. Flytzanis, Phys. Rev. B **42**, 11123 (1990).

[30]J. C. Marini, B. Stebe, and E. Kartheuser, Phys. Rev. B **50**, 14302 (1994).
[31]S. Nomura and T. Kobayashi, Phys. Rev. B **45**, 1305 (1992).
[32]J. J. Shiang, R. H. Wolters, and J. R. Heath, J. Chem. Phys. **106**, 8981 (1997).
[33]P. Kambhampati, Acc. Chem. Res. **44**, 1 (2011).
[34]D. M. Sagar, R. R. Cooney, S. L. Sewall, E. A. Dias, M. M. Barsan, I. S. Butler, and P. Kambhampati, Phys. Rev. B **77**, 235321 (2008).
[35]F. W. Wise, Acc. Chem. Res. **33**, 773 (2000).
[36]T. D. Krauss and F. W. Wise, Phys. Rev. B **55**, 9860 (1997).
[37]T. D. Krauss and F. W. Wise, Phys. Rev. Lett. **79**, 5102 (1997).
[38]W. Kuhn, H. P. Wagner, H. Stanzl, K. Wolf, K. Worle, S. Lankes, J. Betz, M. Worz, D. Lichtenberger, H. Leiderer, W. Gebhardt, and R. Triboulet, Semicond. Sci. Technol. **6**, A105 (1991).
[39]W. Y. Uen, S. Y. Chou, H. Y. Shin, S. M. Liao, and S. M. Lan, Mater. Sci. Eng. B **106**, 27 (2004).
[40]J. Camacho, A. Cantarero, I. Hernandez-Calderon, and L. Gonzalez, J. Appl. Phys. **92**, 6014 (2002).
[41]M. I. B. Utama, Z. P. Peng, R. Chen, B. Peng, X. L. Xu, Y. J. Dong, L. M. Wong, S. J. Wang, H. D. Sun, and Q. H. Xiong, Nano Lett. **11**, 3051 (2011).
[42]K. Saiki, K. Ueno, T. Shimada, and A. Koma, J. Cryst. Growth **95**, 603 (1989).
[43]S. Conesa-Boj, I. Zardo, S. Estrade, L. Wei, P. J. Alet, P. R. I. Cabarrocas, J. R. Morante, F. Peiro, A. Fontcuberta i Morral, and J. Arbiol, Cryst. Growth Des. **10**, 1534 (2010).
[44]L. S. Ramsdell, Am. Mineral. **32**, 64 (1947).
[45]Q. H. Xiong, J. Wang, and P. C. Eklund, Nano Lett. **6**, 2736 (2006).
[46]J. F. Vetelino, S. S. Mitra, and K. V. Namjoshi, Phys. Rev. B **2**, 967 (1970).
[47]K. Sato and S. Adachi, J. Appl. Phys. **73**, 926 (1993).
[48]J. C. Irwin and J. Lacombe, J. Appl. Phys. **41**, 1444 (1970).
[49]P. M. Amirtharaj and F. H. Pollak, Appl. Phys. Lett. **45**, 789 (1984).
[50]D. J. As and L. Palmetshofer, J. Appl. Phys. **62**, 369 (1987).
[51]M. H. Brodsky, J. E. Smith, Y. Yacoby, and R. J. Gambino, Phys. Stat. Sol. B **52**, 609 (1972).
[52]A. S. Pine and G. Dresselh, Phys. Rev. B **4**, 356 (1971).
[53]E. M. Larramendi, G. Berth, V. Wiedemeier, K. P. Husch, A. Zrenner, U. Woggon, E. Tschumak, K. Lischka, and D. Schikora, Semicond. Sci. Technol. **25**, 075003 (2010).
[54]H. Harada and S. Narita, J. Phys. Soc. Jpn. **30**, 1628 (1971).
[55]C. Uzan, R. Legros, Y. Marfaing, and R. Triboulet, Appl. Phys. Lett. **45**, 879 (1984).
[56]J. C. Marini, B. Stebe, and E. Kartheuser, Phys. Rev. B **50**, 14302 (1994).
[57]E. T. Heyen, S. N. Rashkeev, I. I. Mazin, O. K. Andersen, R. Liu, M. Cardona, and O. Jepsen, Phys. Rev. Lett. **65**, 3048 (1990).
[58]A. K. Ganguly and J. L. Birman, Phys. Rev. **162**, 806 (1967).
[59]R. Loudon, Adv. Phys. **13**, 423 (1964).
[60]K. Huang and A. Rhys, Proc. R. Soc. London A **204**, 406 (1950).
[61]T. Takagahara and K. Takeda, Phys. Rev. B **46**, 15578 (1992).
[62]G. W. Bryant, Phys. Rev. B **37**, 8763 (1988).
[63]J. J. Shiang, S. H. Risbud, and A. P. Alivisatos, J. Chem. Phys. **98**, 8432 (1993).
[64]Y. M. Yu, S. Nam, K. S. Lee, Y. D. Choi, and B. O., J. Appl. Phys. **90**, 807 (2001).
[65]R. Merlin, G. Guntherodt, R. Humphreys, M. Cardona, R. Suryanarayanan, and F. Holtzberg, Phys. Rev. B **17**, 4951 (1978).
[66]L. J. Zhao, B. Zhang, Q. Pang, S. H. Yang, X. X. Zhang, W. K. Ge, and J. N. Wang, Appl. Phys. Lett. **89**, 3 (2006).
[67]P. Tyagi, R. R. Cooney, S. L. Sewall, D. M. Sagar, J. I. Saari, and P. Kambhampati, Nano Lett. **10**, 3062 (2010).
[68]P. Tyagi and P. Kambhampati, J. Chem. Phys. **134**, 094706 (2011).
[69]K. W. Adu, Q. H. Xiong, H. R. Gutierrez, G. Chen, and P. C. Eklund, Appl. Phys. A **85**, 287 (2006).
[70]R. Gupta, Q. H. Xiong, G. D. Mahan, and P. C. Eklund, Nano Lett. **3**, 1745 (2003).
[71]Q. H. Xiong, G. Chen, H. R. Gutierrez, and P. C. Eklund, Appl. Phys. A **85**, 299 (2006).
[72]V. M. Dzhagan, I. Lokteva, M. Y. Valakh, O. E. Raevska, J. Kolny-Olesiak, and D. R. T. Zahn, J. Appl. Phys. **106**, 6 (2009).
[73]E. Stock, M. R. Dachner, T. Warming, A. Schliwa, A. Lochmann, A. Hoffmann, A. I. Toropov, A. K. Bakarov, I. A. Derebezov, M. Richter, V. A. Haisler, A. Knorr, and D. Bimberg, Phys. Rev. B **83**, 041304(R) (2011).
[74]S. Hughes, P. Yao, F. Milde, A. Knorr, D. Dalacu, K. Mnaymneh, V. Sazonova, P. J. Poole, G. C. Aers, J. Lapointe, R. Cheriton, and R. L. Williams, Phys. Rev. B **83**, 165313 (2011).
[75]D. Sarkar, H. P. van der Meulen, J. M. Calleja, J. M. Meyer, R. J. Haug, and K. Pierz, Phys. Rev. B **78**, 241305 (2008).
[76]G. Bester, X. F. Wu, D. Vanderbilt, and A. Zunger, Phys. Rev. Lett. **96**, 187602 (2006).
[77]C. B. Duke and G. D. Mahan, Phys. Rev. **139**, 1965 (1965).
[78]I. Favero, G. Cassabois, R. Ferreira, D. Darson, C. Voisin, J. Tignon, C. Delalande, G. Bastard, P. Roussignol, and J. M. Gerard, Phys. Rev. B **68**, 233301 (2003).
[79]Y. Liu, R. Sooryakumar, E. S. Koteles, and B. Elman, Phys. Rev. B **45**, 6769 (1992).
[80]S. Nakashima, T. Hattori, and Y. Yamagudi, Solid State Commun. **25**, 137 (1978).
[81]W. Maier, G. Schmieder, and C. Klingshirn, Z. Phys. B **50**, 193 (1983).
[82]E. S. Koteles and G. Winterling, Phys. Rev. B **20**, 628 (1979).
[83]R. M. Martin and C. M. Varma, Phys. Rev. Lett. **26**, 1241 (1971).